https://doi.org/10.5194/egusphere-2026-2675
Preprint. Discussion started: 21 May 2026

MethaneSAT instrument spectral response functions during pre-launch calibration and on-orbit performance

David J. Miller[1,2,3], Kang Sun[1], Jonathan E. Franklin[3], Nathan Leisso[4], Sébastien Roche[3,5], Bingkun Luo[2], Christopher Chan Miller[2,5], Sasha Ayvazov[5], Sean Crowell[6], Nick LoFaso[5], Tom Kampe[4], Peter Spuhler[4], Betsy Farris[4], Eleanor Walker[3], Tom Melendez[5], Ritesh Gautam[5], Xiong Liu[2], and Steven C. Wofsy[3]

[1] Department of Civil, Structural and Environmental Engineering, University at Buffalo, Buffalo, NY, USA
[2] Center for Astrophysics | Harvard & Smithsonian, Cambridge, MA, USA
[3] Harvard John A. Paulson School of Engineering and Applied Sciences, Harvard University, Cambridge, MA, USA
[4] BAE Systems, Inc., Boulder, CO, USA
[5] Environmental Defense Fund, New York, NY, USA
[6] Department of Earth and Environmental Sciences, University of Rochester, Rochester, NY, USA
Correspondence to: David J. Miller (djmtwo@alumni.princeton.edu)

Abstract. MethaneSAT was a push-broom, area-mapping satellite that quantified area and point source methane (CH_4) emissions across global target areas. Two sensors onboard MethaneSAT measured short-wave infrared absorption bands of CH_4, carbon dioxide, and oxygen. We report novel methods for MethaneSAT spectral calibration during pre-launch measurements and on-orbit operation. We derive and compare instrument spectral response functions (ISRFs) measured during ground calibrations at the individual sensor level at three temperatures and at the integrated flight system level. Point spread functions are used to develop peak and ghost stray-light kernels. Underlying line shape exposures were stray-light corrected based on these kernels prior to deriving ISRFs. Novel methods robustly merge ISRFs at three overlapping slit illumination fields of view and identify bad ISRF positions for gap filling. We evaluate four distinct ISRF data sets for on-orbit calibration across three different thermal conditions by squeezing the ISRF in level 2 (L2) retrievals. ISRF widths varied by <5% between calibration experiments across a wider range of thermal environments than those observed on-orbit. The use of ISRFs measured at temperatures closest to those observed on-orbit resulted in a value close to unity for the parameter that squeezes the ground-based calibration derived ISRFs in L2 retrievals. A time series of these squeeze factor deviations demonstrate relatively stable on-orbit spectral calibration across the mission duration with <0.4% variations. Our results demonstrate stable on-orbit instrument spectral response and on-orbit wavelength shift variations compared with ground-based calibration across expected on-orbit thermal conditions. These results support the high accuracy and stability of MethaneSAT L2 retrievals.

https://doi.org/10.5194/egusphere-2026-2675
Preprint. Discussion started: 21 May 2026

1 Introduction

MethaneSAT was a push-broom, area-mapping satellite launched into sun-synchronous orbit on March 4, 2024 that was operational with on-orbit data collection until June 20, 2025. To mitigate climate change with a focus on relatively short-lived greenhouse gas emissions, the MethaneSAT mission aims to catalyze oil and gas methane (CH_4) emission reductions by quantifying discrete and dispersed CH_4 emission sources (Williams et al., 2026). MethaneSAT operated among a suite of related, high spectral resolution shortwave infrared (SWIR) instruments retrieving greenhouse gases, including TROPOMI (van Hees et al., 2018; van Kempen et al., 2018), OCO-2, OCO-3 (Crisp et al., 2017; Taylor et al., 2020), GOSAT, GOSAT-2 and the recently launched GOSAT-GW (Tanimoto et al., 2025). MethaneSAT's unique capabilities, including a large format 2048 x 2048 pixel focal plane array (FPA) for each sensor, high spatial resolution on the ground (~ 100 m x 400 m), large basin-scale swath width (220 km at nadir) and high retrieval precision (20-35 ppb), filled a critical gap between target mode and global mapping on-orbit CH_4 sensing satellites (Nasr et al., 2025). MethaneAIR, the airborne simulator of MethaneSAT, was designed and validated to demonstrate and test pre-launch MethaneSAT capabilities and algorithms with a similar spectrometer design (Staebell et al, 2021; Chulakadabba et al., 2023; Chan Miller et al., 2024; Conway et al., 2024). MethaneAIR continues to demonstrate novel capabilities to apportion CH_4 emission point and area sources across U.S. oil and gas basins (Warren et al., 2025; MacKay et al., 2026).

Accurate instrument spectral response function (ISRF) estimation for the MethaneSAT spectrometers is essential to ensure accurate retrievals. The ISRF represents the response of one spectral pixel to photons at different wavelengths. Level 2 (L2) retrieval algorithms typically convolve the ISRF with reference spectra, and ISRF uncertainties are dominant sources of retrieval errors (e.g. van Hees et al., 2018; Chan Miller et al., 2024). Staebell et al. (2021) presented the spectral calibration of MethaneAIR, serving as a pathfinder and roadmap for new spectral calibration methods required for MethaneSAT. Pre-launch spectral response functions are typically characterized using tunable diode laser-based slit illumination measurements and solar absorption spectra (e.g. Lee et al., 2017; van Hees et al., 2018). ISRFs are often derived via parameterizations assuming a Gaussian or a related analytical functionality that varies smoothly in the spatial and spectral directions (e.g. van Hees et al., 2018), sparse representation based on linear combinations of an ISRF dictionary at a small number of central wavelengths (El Haouari et al., 2025), or an empirical fitting of measured line shapes at a collection of discrete central wavelengths and spatial pixels (e.g. Lee et al., 2017; Staebell et al., 2021). Furthermore, it is important to distinguish spectral stray-light from the ISRF extent and apply a correction to redistribute stray-light prior to ISRF estimation. Point spread function measurements are useful to derive stray-light kernels, including reflective spatial ghost features, for this important correction (Tol et al., 2018).

On-orbit Instrument Line Shape (ILS) monitoring is also important to evaluate stability and drift compared with pre-launch calibrations. TROPOMI was designed for on-orbit ILS monitoring using on-board lasers (van Kempen et al., 2019). OCO-2 was designed with a solar diffuser for measuring solar irradiance spectra to monitor ILSs (Crisp et al., 2017; Sun et al., 2017).

https://doi.org/10.5194/egusphere-2026-2675
Preprint. Discussion started: 21 May 2026

Crisp et al. (2017) also report the fitted on-orbit wavelength shift and wavelength grid (dispersion) stretch parameters as metrics of on-orbit spectral calibration stability, finding these parameters are well correlated with temperatures and temperature gradients that introduce defocusing effects. However, dispersion stretch factors cannot fully account for second-order ISRF shape changes associated with thermal defocusing effects. Due to mission constraints, MethaneSAT ground-based calibration did not include solar heliostat measurements. Furthermore, MethaneSAT was designed without a solar diffuser or on-board lasers for on-orbit ISRF monitoring, requiring alternative approaches to monitor on-orbit stability. The approach implemented for MethaneSAT L2 retrievals involves retrieving three squeeze factor parameters relative to the pre-launch ISRFs within the state vector for the carbon dioxide (CO_2), CH_4 and oxygen (O_2) spectral fit windows (Staebell et al., 2021; Chan Miller et al., 2024). Therefore, it is important to characterize the spatial and spectral patterns in ISRF shape with careful ground-based measurements and to assess their corresponding L2 metrics during on-orbit measurements.

In this study, we present novel methods to estimate ISRFs based on pre-launch calibration, evaluate on-orbit spectral calibration metrics, and investigate thermal defocusing impacts on ISRFs and retrievals. We focus on ground-based thermal vacuum chamber calibration measurements at the individual sensor level conducted at three temperatures, and at the integrated flight system level at nominal operational temperature. Our main objective is to demonstrate novel pre-launch ISRF and wavelength calibration estimation methods. The large spatial extent of MethaneSAT spectrometers presented challenges for ground-based calibration measurements, including limited overlap between three illuminated fields of view. We develop a new method to merge ISRFs at overlapping spatial pixel positions based on exponential signal-weighted median. Next, we characterize the temperature dependence of ISRF shape as well as calibration experiment differences. Finally, we examine fitted wavelength shift and ISRF squeeze factor parameters in clear sky, bright on-orbit MethaneSAT scenes to assess on-orbit ISRF accuracy and stability.

2 Methods

2.1 MethaneSAT overview and its pre-launch calibration

The MethaneSAT instrument design and radiometric calibration are described in detail by Rohrschneider et al. (2021) and Luo et al. (2025), respectively. MethaneSAT spectrometer specifications and spectral fitting window metrics are shown in Table 1. Level 0 to 1B algorithms are reported by Conway et al. (2024) and Luo et al. (2025). The MethaneSAT L2 retrieval algorithm has been introduced by Chan Miller et al. (2024), and the on-orbit L2 retrieval performance is the subject of a separate, upcoming study. Briefly, one spectrometer covers an CH_4 absorption window centered at 1.66 μm with 0.08 nm per pixel dispersion and 0.23 nm full width at half maximum (FWHM). Although not originally designed to cover the CO_2 band, this spectrometer also covers a CO_2 absorption window at 1.61 μm with 0.08 nm per pixel dispersion and 0.25 nm FWHM. While the CO_2 band is used for retrievals and we distinguish this band for spectral calibration, the instrument design did not aim to

https://doi.org/10.5194/egusphere-2026-2675
Preprint. Discussion started: 21 May 2026

control the CO_2 band spectral distortion parameters. Therefore, we expect performance differences between the CH_4 and CO_2 spectral bands. A second spectrometer covers an O_2 absorption window centered at 1.27 μm, with 0.06 nm per pixel dispersion and 0.16 nm FWHM. We derived the MethaneSAT ISRFs at each usable spatial pixel and selected central wavelengths to cover the spectral fitting windows for CH_4, CO_2, and O_2 retrievals. The ISRF estimation methods follow those reported for MethaneAIR by Staebell et al. (2021), with several key refinements for MethaneSAT presented in this section.

Specification	CH_4, CO_2 spectrometer	O_2 spectrometer
Passband (nm)	1598 to 1683	1249 to 1305
L2 retrieval bands (nm)	1598 to 1618 (CO_2) 1629 to 1654 (CH_4)	1249 to 1288 (O_2)
Dispersion (nm pixel^{-1})	0.08	0.06
Median spectral FWHM (nm)	0.25 (CO_2) 0.23 (CH_4)	0.16
Calibration window spectral pixel range	720 to 2030	720 to 2030
Science window spectral pixel range	880 to 1967	816 to 1807
Usable spatial pixel range	35 to 2013	32 to 2018
Point spread function FWHM (spatial pixels)	1.8	1.5

Table 1: MethaneSAT spectrometer specifications and spectral fitting windows. Spectral resolution and spatial point spread function FWHM values are derived based on methods described in section 2

Pre-launch, ground-based MethaneSAT ILS calibration measurements were conducted at both sensor and flight system levels via diffuse illumination of the 54 μm width slit with Santec TSL-550 Type C tunable diode lasers. ILS is a frame of the FPA exposed to laser photons at a fixed wavelength and wide spatial coverage. An integrating sphere was used to illuminate a kinematically mounted spatial target placed at the focus of an off-axis parabolic mirror that fed collimated light into the thermal vacuum chamber (TVAC). Because only a fraction of the slit could be illuminated at one time, a TVAC gimbaled Spectralon panel on the other side of the gimbaled holder was used to illuminate ~33% of the field of view. The Spectralon panel diffuses the light and enables simultaneous capture along a portion of the spatial extent.

All pre-launch calibration activities were conducted at Ball Aerospace (Ball Aerospace is now BAE Systems) in Boulder, Colorado. We conducted two MethaneSAT sensor level ILS calibration experiments. The first sensor level ILS characterization included only three central wavelengths and six spatial positions. The second sensor level characterization, referred to as sensor-level “goBack,” was conducted during March-May 2022 and is used in the present study. During sensor level goBack

https://doi.org/10.5194/egusphere-2026-2675
Preprint. Discussion started: 21 May 2026

testing, ILSs were collected at three different temperatures: “cold” (19.25 °C), “nominal” on-orbit operation (19.5 °C) and “warm” (19.75 °C). This temperature range represents the maximum expected on-orbit seasonal variations from the mission beginning through end of life. Speckle from the tunable lasers was expected and attempts were made during sensor level calibrations to mitigate its impact. Specifically, the SanTec lasers were operated in “coherence control” mode where the laser line was slightly dithered. In addition, the lasers were fiber-fed to a piezo driven diffuser at the entrance port of the integrating sphere. While these methods reduced speckle, the combination of coherence control and the piezo-driven diffuser did not fully mitigate speckle due to the tight coherence of the lasers. Subsequently, MethaneSAT flight system level ILS calibrations were conducted at nominal expected on-orbit operating temperature (19.5 °C) during December 2023. At flight system level, we aimed to further mitigate residual speckle relative to the approaches during sensor level calibrations by also using an in-line fiber optic de-speckler (Newport, Inc.). We removed the integrating sphere and used the piezo-driven diffuser behind the spatial target. The laser fiber was also repositioned to directly illuminate the diffuser to provide higher signal and reduce the integration time from 480-ms to the flight integration time of 56.35-ms. However, this slightly increased speckle noise relative to sensor level goBack calibrations.

Thermal conditions during ILS measurements were characterized by multiple thermistor measurements across the sensor and flight systems. We focus on the following subset of thermistors relevant for the present study. During sensor level calibrations, the sensor objective lens and spectrometer temperatures were controlled through Ground Support Equipment (GSE) thermistors objective element 1 and spectrometer element 2, respectively. Spectrometer and objective temperatures are expected to be indicators of thermal defocusing effects because the spectrometer reimages the slit onto the FPA. The MethaneSAT spectrometers include compensating prisms to correct for spectral smile and anamorphic magnification. Prism temperatures were also measured within each spectrometer. A 1.8°C thermal gradient was maintained between the spectrometer and objective to balance heater loads. The temperature precisions are $< \pm 0.05$°C due to heater control cycles. For flight system level calibration, we adjusted the flight bench heater and objective heater setpoint to drive the GSE heaters objective element 1 and spectrometer element 2 to the same temperature as during sensor level calibrations. This setpoint was locked in as the flight setpoint. We attempted to minimize thermal condition differences between sensor level goBack and flight system level measurements. The thermistors introduced above remained in the same locations for all ground-based calibrations. However, the thermal environment was somewhat different between sensor level goBack and flight system level measurements. During sensor level goBack calibrations, the sensors were in a TVAC chamber and the FPAs were cooled through a cryo-cooler and cold bar, resulting in the sensors being more sensitive to the ambient thermal conditions of the chamber. During flight system level calibration, the sensors were integrated, Multi-Layer Insulation was installed, the TVAC chamber was better thermally controlled, and the FPAs were cooled through the radiator that was more representative of flight conditions.

https://doi.org/10.5194/egusphere-2026-2675
Preprint. Discussion started: 21 May 2026

ILS exposure collections at three spatial fields of view were used to estimate ISRFs. At 17 central wavelengths from 1598 nm through 1683 nm (CH_4 sensor) and 14 central wavelengths from 1253 nm through 1305 nm (O_2 sensor), we used micro-wavelength steps collected across 0.16 nm (CH_4) and 0.10 nm (O_2) ranges about each central wavelength at 0.01 nm (CH_4) and 0.008 nm (O_2) resolution steps (Table 2). We excluded the O_2 sensor ILS collected at 1249 nm due to a reduced signal to noise ratio because the tunable lasers had approximately one third of the output signal level at their spectral range edges compared with that at their spectral range center. At flight system level, micro-wavelength steps were collected at sensor level goBack step sizes for the nadir position, whereas a "Lite" version at 50% coarser step size was collected for the off-nadir spatial positions (Table 2). The "Lite" version was collected instead of the full version due to data transfer and experimental duration constraints. For comparison across experiments, we subsampled micro-wavelength steps at sensor level goBack to be consistent with the micro-wavelength step size sampled at flight system level. Specifically, to match spectral step resolutions with CH_4 sensor flight system level spatial fields 2 and 6, micro-wavelength steps were sub-sampled by a factor of two in all other experiments. To match spectral step resolutions with O_2 sensor flight system level spatial field 2, micro-wavelength steps were sub-sampled by a factor of two in all other experiments. Sensitivity analyses with micro-wavelength resolutions ranging from that at native sensor level goBack to a factor of 3 coarser resolution showed comparable ISRF fitting root-mean squared error (RMS) and number of fitting iterations. We computed the mean of exposure scans for a given collect, followed by subtracting the corresponding dark collect. These mean exposures were smoothed using the median signal across 20 (CH_4) and 10 (O_2) spatial pixel moving windows to mitigate the impacts of laser speckle noise. Bad pixels were identified and masked based on flight system level Operational Test Group 1 dark current collects (−85 °C FPA temperature), electronic offset noise, and the most extreme random telegraph signal offsets.

ILS experiment	Integration time (ms)	Frame rate (frames s^{-1})	Native micro-wavelength step size (nm)	Subsampled micro-wavelength step size (nm)	Micro-wavelength step range (nm)	Exposure level smoothing window (spatial pixels)
CH_4 sensor level goBack	500	1.8	0.005	0.010	0.16	20
CH_4 flight system level	56.35	17.5	0.005 (nadir) 0.01 (off-nadir)	0.010	0.16	30
O_2 sensor level goBack	700	1.3	0.004	0.008	0.10	10
O_2 flight system level	56.35	17.5	0.004 (nadir) 0.008 (off-nadir)	0.008	0.10	10

Table 2: Specifications of sensor level goBack and flight system level experiments used to derive ISRFs. Nadir refers to spatial field 4 and off-nadir refers to spatial field 2 and/or 6.

https://doi.org/10.5194/egusphere-2026-2675
Preprint. Discussion started: 21 May 2026

2.2 Stray-light kernels and correction

Point spread functions (PSFs) were collected only during sensor-level goBack calibrations at nominal operating temperature. Seven spatial field positions for each sensor were subsequently illuminated with Santec tunable diode laser light incident on a pinhole target. A 3-axis gimbaled fold mirror was used to precisely position (or scan) the collimated input relative to the sensor that enabled "point-source" illumination for PSF collections. Coherence control was implemented by dithering the laser line to reduce coherence noise. For in-band PSFs, lasers were stepped from 1610 to 1678 nm in 17 nm increments for the CH_4 sensor and stepped from 1253 to 1301 nm in 12 nm increments for the O_2 sensor. Four PSF exposure collections were conducted at 10 ms, 100 ms, 1000 ms and 9950 ms integration times to capture the full dynamic range of PSF peak and tail structure. Twenty frames per collect were measured due to instability of the first few frames after an integration time change.

We derived peak and reflective ghost stray-light kernels using the PSF collections based on methods reported in Staebell et al. (2021) and Tol et al. (2018). First, background subtracted mean frames per exposure time were combined based on four individual PSF exposure sets acquired at different integration times following Staebell et al. (2021). Next, we merged PSF exposures in the spectral direction at four of the spatial pixel peak positions (2, 3, 5 and 6) via the median values at each pixel on a common interpolated grid (Figure 1). We aligned the PSFs based on their centers of mass in both the spatial and spectral directions. For MethaneSAT, stray-light kernels were developed separately for the peak and a reflective ghost stray-light feature in the PSF collects. The ghost feature is offset from the peak in the spatial direction and is ~5 orders of magnitude lower than the peak signal (Figure 1). The sum of the centers of mass for peak and ghost features is a constant for each sensor in both the spatial and spectral directions, though spectral pixel centers of mass between peak and ghost features were identical for both sensors. We limited the spatial pixel peak positions to 2, 3, 5 and 6 (Figure 1) to ensure that peak and ghost features were distinctly separated in the spatial direction, eliminating spatial positions in which PSF peak and ghost features are overlapping with either each other or the spatial pixel edges.

https://doi.org/10.5194/egusphere-2026-2675
Preprint. Discussion started: 21 May 2026

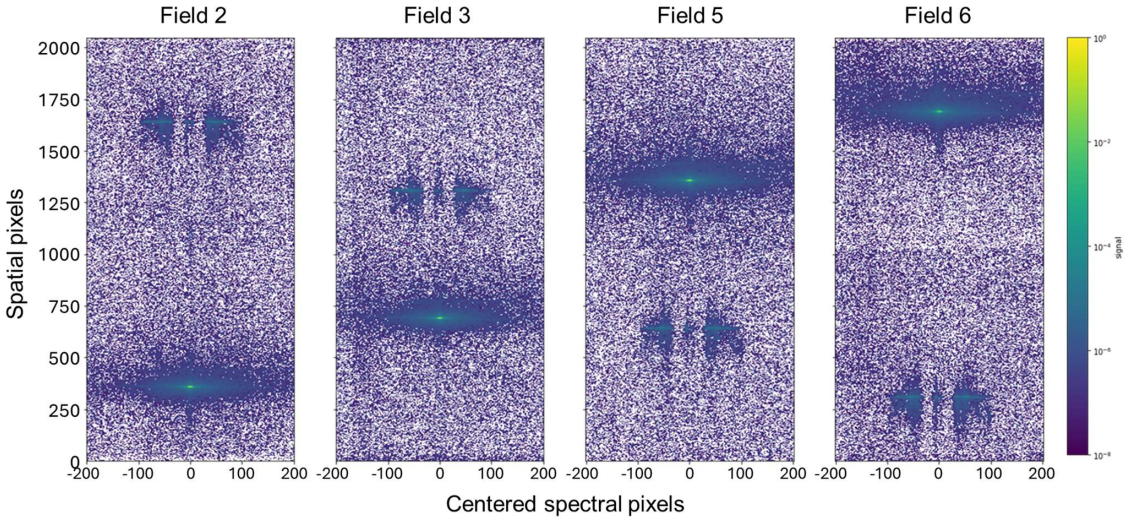

Figure 1. Peak-normalized, background-subtracted CH_4 sensor level goBack point spread function exposures.

Several key method refinements were incorporated for MethaneSAT stray-light kernel derivation (Figure 2) relative to MethaneAIR (Staebell et al., 2021). We accounted for variable exposure backgrounds in PSF measurements associated with thermal self-emission from the detector housing by fitting and subtracting a two-dimensional plane baseline for each exposure collection. For the peak kernel, we use ± 500 pixels from the peak center in both spatial and spectral directions. For the ghost kernel, we use -500 to +200 pixels from the ghost center. We mask near-field pixels in the peak kernel to estimate the far-field kernel based on spatial point spread function at 10^{-3} below peak, corresponding to ± 6 spatial pixels from peak center in both sensors. The spectral range for ISRF beyond which spectral stray-light dominates the signal was determined by examining the ISRF without stray-light correction. For both sensors, the ISRF ends beyond ± 7 spectral pixels and transitions to spectral stray-light. We masked ± 7 near-field spectral pixels in the peak kernel to account for the ISRF extent. Outside of the ISRF extent, ISRF values were set equal to zero to avoid spurious detector noise spikes at ISRF tails.

https://doi.org/10.5194/egusphere-2026-2675
Preprint. Discussion started: 21 May 2026

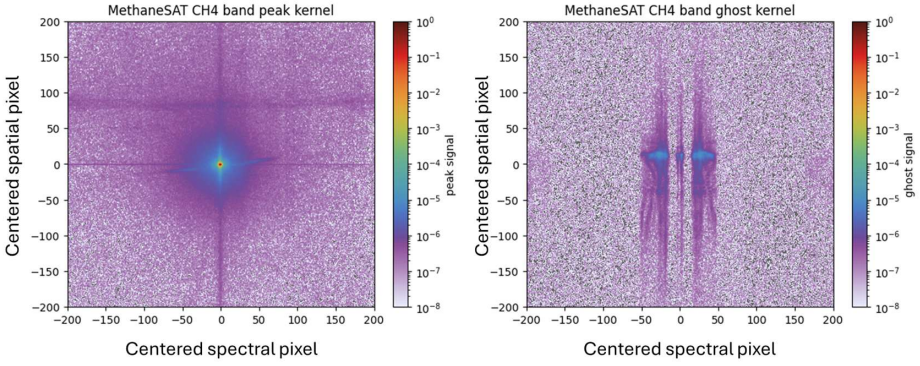

(a)

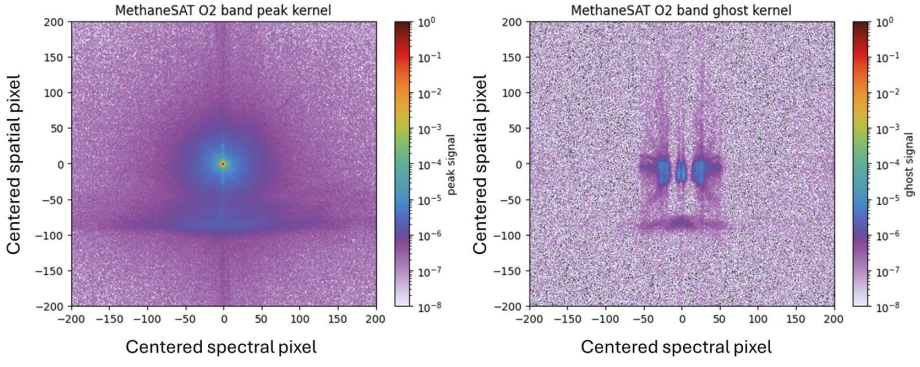

(b)

Figure 2. Peak and ghost far-field stray-light kernels for MethaneSAT (a) CH_4 and (b) O_2 sensors, normalized to the peak kernel maximum value.

In-band stray-light correction via iterative deconvolution (n=2 iterations) with the far-field stray-light kernel followed by deconvolution with the reflective ghost kernel was applied to each exposure frame used in this study at all usable spatial pixels, consistent with methods detailed by Tol et al. (2018). This method redistributes light in the far-field defined as the area beyond the extent of the spatial PSF in the spatial direction and the ISRF extent in the spectral direction. We set reflective edge padding at 100 pixels from the frame edges in both the spatial and spectral directions to ensure continuity at the kernel edges while minimizing the number of pixels to optimize algorithm run-time. We temporarily set permanent bad and overexposed pixels to an undefined missing value prior to stray-light correction; at these pixels we interpolate a value prior to deconvolution using the stray-light kernel as the interpolation function. We include the ghost kernel in the stray-light correction in all exposure

https://doi.org/10.5194/egusphere-2026-2675
Preprint. Discussion started: 21 May 2026

collections because it impacts the near-nadir spatial field 4 exposures where the spatial ghost overlaps with the slit illumination. Deconvolution of the effective ghost stray-light kernel includes spatial pixel direction mirroring and spectral pixel shifting of the ghost kernel with respect to the peak kernel following Tol et al. (2018). An example of ILS exposure frames before and after stray-light correction are depicted in Figure 3.

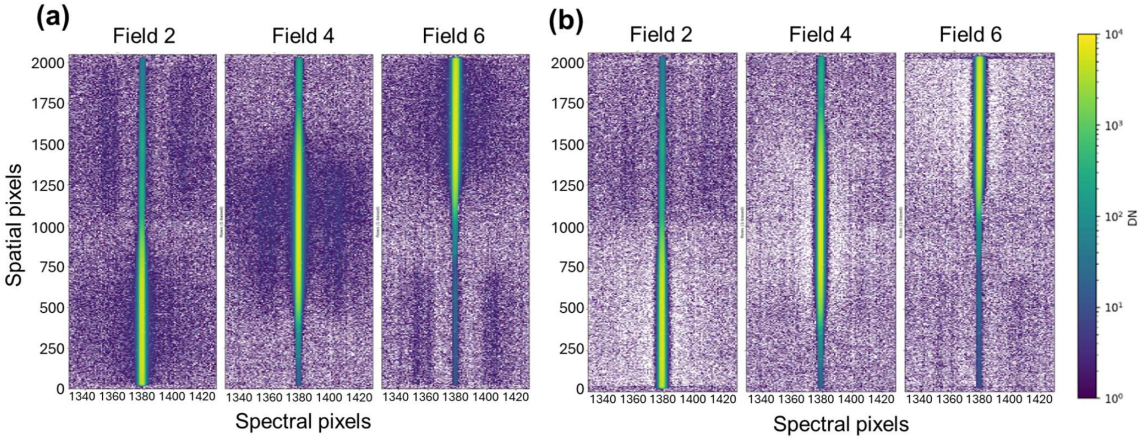

Figure 3: Exposure frame example for CH_4 sensor level goBack nominal temperature ILS at 1643.85 nm (a) prior to stray-light correction, and (b) after stray-light correction. Distinct illuminated spatial fields of view across the length of the slit are labeled 2, 4 and 6.

A metal bezel was positioned in close proximity to the FPA active area and covered spatial edge pixels. The bezel edge was illuminated during ILS measurements because the slit extended beyond the bezel. Usable spatial pixel extents were determined based on the spatial response of bezel edge pixels to a PSF with its center incident near the bezel edge. Bezel scattering effects for illuminated spatial pixels beyond the PSF width itself may lead to spurious radiance artifacts and secondary PSF peaks that are not easily removed by the stray-light correction. We compare the intended target spatial pixel with the detected peak spatial pixel for each collect. The peak spatial position is biased towards the FPA center direction compared with the target due to bezel scattering effects. A larger scattering effect occurs when the PSF target is closest to the bezel edge. Based on the spatial responses, we expect two effects to occur at a given spatial pixel near the bezel edge. First, the peak radiance will be biased low relative to the true radiance due to scattering into adjacent spatial pixels. Second, the radiance at a given spatial pixel can be enhanced due to scattering of light incident closer to or even under the bezel. The spatial pixel where these effects become negligible compared with the PSF spatial response itself defines the usable spatial pixel extent. We find the bezel scatter extends from the bezel edge into the FPA by 16-17 spatial pixels (CH_4 sensor) and by 10 spatial pixels (O_2 sensor).

https://doi.org/10.5194/egusphere-2026-2675
Preprint. Discussion started: 21 May 2026

2.3 ISRF fitting

The series of instrument spectral spread functions (ISSFs) at individual micro-wavelength steps was oversampled based on methods reported in Staebell et al. (2021). ISRFs were defined at ± 1.5 nm from peak center with 0.0005 nm resolution. We fit ISRFs using an iterative, third order Savitzky–Golay filter with n=29 (CH_4) and n=31 (O_2) window lengths optimized for each spectrometer to capture ISRF shape, while also suppressing measurement noise (Fig. 4). This numerical fitting approach was applied due to the complex ISRF shapes that are not easily described by analytical functions. Additional ISRF fitting method innovations were implemented relative to those for MethaneAIR. Specifically, the ISRF construction was iterative with convergence criteria, while the maximum iteration was set at 20. For each iteration, the oversampled profile was smoothed by the Savitzky–Golay filter, and then each ISSF was fitted to update its location. This produced higher quality ISRFs and more precise load dispersion as discussed in section 3.2.

We merged three fields of view (FOV) of the slit illumination (Figure 3) due to the relatively large spatial pixel extents of the MethaneSAT spectrometers. Due to the limited overlap between the three illumination FOVs, we implemented a discontinuity reduction approach. ISRFs at overlapping spatial pixels were merged via the inverse fourth-power exponential signal-weighted median using carefully chosen spatial pixel extents for each FOV to provide smooth transitions and minimize the influence of FOV edge stray-light artifacts. The weighting equations (1) and (2) for the merged ISRF at a specific spatial pixel ($isrf\,(s)$) are as follows:

$$w_1 = D^i \; ; \; w_2 = 1 \,/\, D^i \quad (1)$$

$$isrf\,(s) = (w_1 * isrf_1\,(s) + w_2 * isrf_2\,(s)\,) \,/\, (w_1 + w_2) \quad (2)$$

where s is a given spatial position; D is the maximum scale-normalized absolute difference between mean scales of overlapping ISRFs; $isrf_1$ and $isrf_2$ are ISRFs at the same spatial position with different fields of view; and w_1 and w_2 are their corresponding weights. Different weighting exponents (i) were tested; i=4 produced the smoothest results.

https://doi.org/10.5194/egusphere-2026-2675
Preprint. Discussion started: 21 May 2026

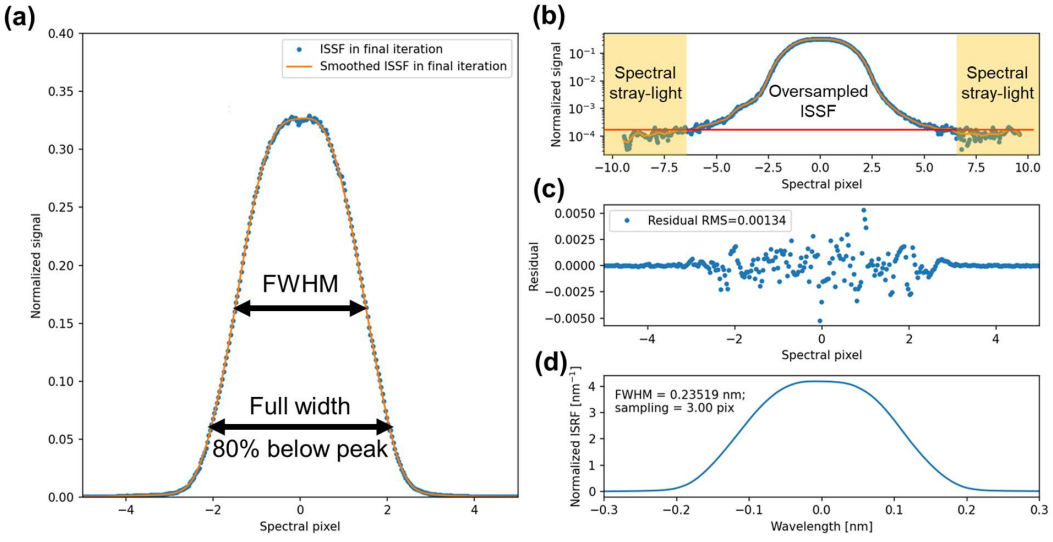

Figure 4: (a) Oversampled ISSF at central wavelength of 1649.5 nm and spatial pixel 40, with fitting at final iteration (n=5). Relevant width metrics are denoted and presented in section 3.1. (b) Oversampled ISSF, same as in (a), on a log scale. The horizontal red line indicates the level of spectral stray-light, (c) Fitting residuals and root mean squared error (RMS) metric of oversampled ISSF fit. (d) Normalized ISRF corresponding to (a) and (b) using local dispersion (0.0783 nm pixel^{-1}) to determine the wavelength axis. Global wavelength calibration updates this axis in subsequent steps. Differences between local and global dispersion are examined in section 3.2.

Outlier ISRF positions were identified via (1) exceedance of two standard deviations in the deviation in RMS from median RMS, where RMS is computed based on comparing each ISRF to the median ISRF in a 50 spatial pixel window, (2) zero or missing ISRF widths, and (3) outlier ISRF widths exceeding the 75th percentile plus 1.5 times the interquartile range in a 50 spatial pixel moving window. These outlier criteria identified bad ISRF positions due to factors including fitting issues or bad pixels not captured in earlier masking. To ensure that the ISRFs have a smooth spatial pixel gradient that is physically expected, bad positions were masked and gap-filled using the median non-outlier ISRFs at 30 nearest neighbor spatial pixels.

2.4 Wavelength calibration

Wavelength registration was performed using the center spectral pixels based on a center of mass calculation. No additional smoothing was performed for the center spectral pixel due to the exposure level spatial pixel smoothing that sufficiently suppressed noise spikes. The spectral smile was evaluated using the deviation from median center spectral pixel and was found

https://doi.org/10.5194/egusphere-2026-2675
Preprint. Discussion started: 21 May 2026

to be central wavelength dependent. For the wavelength calibration curve, a third order polynomial fitting was chosen based on minimum values of the spatial pixel ensemble of Akaike and Bayesian Information Criteria parameters. To ensure smooth wavelength calibration coefficients in the spatial pixel direction, we flagged outlier wavelength calibration coefficients based on exceedance of one standard deviation above a third-order Savitzky–Golay filter with 150 (CH_4) or 200 (O_2) spatial pixel windows. Each coefficient was evaluated with respect to the outlier criterion. If at least one coefficient was identified as an outlier, all coefficients for the given spatial pixel were gap-filled using the nearest 30 spatial pixel moving window of non-outlier median coefficients. A wavelength calibration coefficient lookup-table is used to initialize the wavelength grid within the L1A process. Then, we used a cross-correlation method to determine an initial guess of the wavelength grid shift to the nearest spectral pixel (Chan Miller et al., 2024). Finally, a wavelength offset was fitted in the L2 retrieval with an accuracy better than that of the spectral computation grid of 0.01 nm (CH_4 sensor) or 0.002 nm (O_2 sensor).

3 Results

3.1 ISRF FPA patterns and temperature dependence

Peak-normalized ISRF shapes and their spatial and central wavelength gradients across the four experiments and three thermal conditions are generally consistent and exhibit relatively minor sensitivities to thermal defocusing within the range tested (Figs. 5, 6 and 7). ISRF widths in the four different calibration experiments generally show <1% width variations and ~5% spatial pixel gradient in ISRF width, except for ~5% width variations and ~10% spatial pixel gradient in the CO_2 band (Fig. 8). We used the CH_4 spectrometer cold temperature sensor level goBack and the O_2 spectrometer flight system level derived ISRFs for subsequent analyses; further explanation on this choice is detailed in section 3.3. Sensor level temperature effects on ISRF widths show spatial pixel pattern differences generally in opposite directions at tails compared with closer to the peak (Figs. 5 and 6). We observe asymmetric temperature effects on ISRF width with larger relative differences between warm and nominal temperature compared with that between cold and nominal temperature (Fig. 8). ISRFs near spatial pixel and spectral window edges exhibit noise features in the ISRF wings that are relatively small speckle noise features minimized by exposure level spatial pixel smoothing (Figs. 5 and 6).

Flight system level ISRF shapes and widths are within family compared with those collected during sensor level goBack calibrations (Figs. 5 and 6). However, at flight system level, the spatial pixel edges of each illumination spatial FOV exhibited unusual patterns with broadened ISRFs; this effect is especially pronounced in the CO_2 band (Fig. 8). The artifacts in the ILS measurements at the illumination edges are stronger and more prominent at the flight system level and in the CO_2 band. These artifacts align with the scatter profile of the high dynamic range PSF collections on the bezel edge and are discussed further in section 3.3.

https://doi.org/10.5194/egusphere-2026-2675
Preprint. Discussion started: 21 May 2026

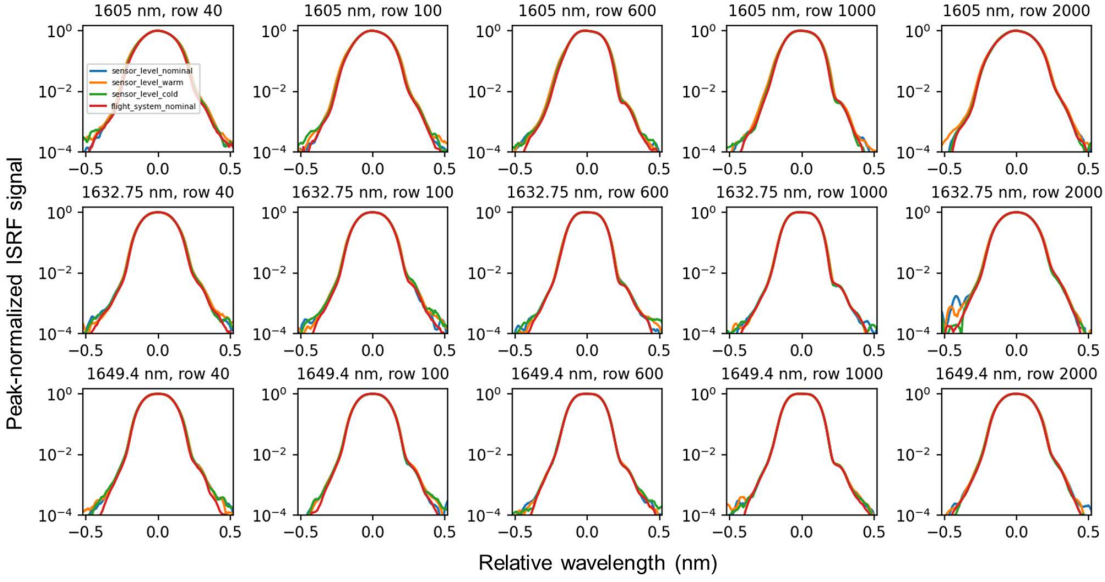

Figure 5: CH_4 and CO_2 band ISRF shapes at three central wavelengths covering the CH_4 and CO_2 spectrometer spectral fitting windows and five spatial pixel positions, including <5 pixels from spatial pixel edge.

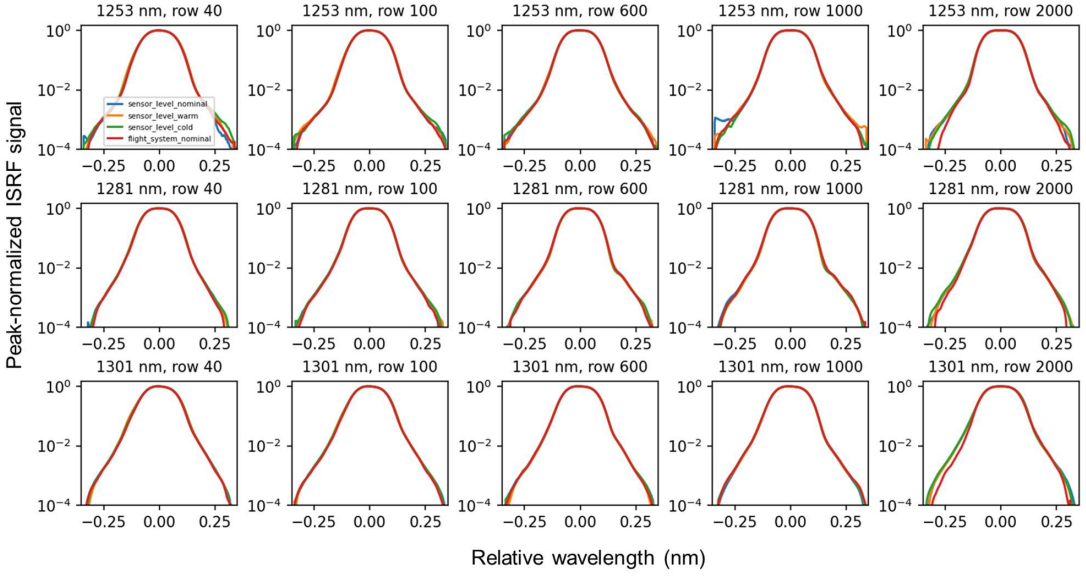

https://doi.org/10.5194/egusphere-2026-2675
Preprint. Discussion started: 21 May 2026

Figure 6: O_2 band ISRF shapes at three central wavelengths covering the O_2 spectrometer spectral range and five spatial pixel positions, including <5 pixels from spatial pixel edges.

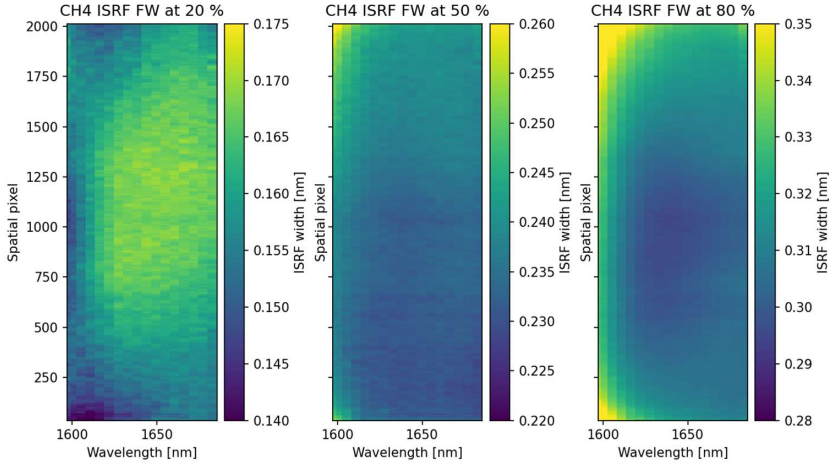

Figure 7: ISRF widths at 20%, 50% and 80% below peak, at cold sensor level (CH_4 and CO_2 band above) and at flight system level (O_2 band below).

https://doi.org/10.5194/egusphere-2026-2675
Preprint. Discussion started: 21 May 2026

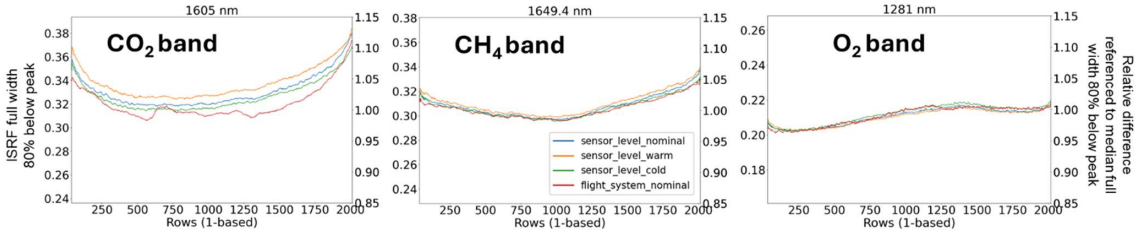

Figure 8: ISRF widths at 80% below peak, a measure of the ISRF tail, at three central wavelengths at the three fitting band centers, across each of four experiments.

3.2 Wavelength calibration

The wavelength calibration curves illustrate the high precision of the wavelength grid across the FPA prior to L2 retrieval. Specifically, wavelength calibration fitting residuals are <1.3% (CH_4 and CO_2 band) and <1.2% (O_2 band) of one spectral pixel (Fig. 9). Wavelength calibration curves exhibit a similar residual fit level at spatial pixel edges compared with the middle of the FPA. Akaike Information Criterion (AIC) and Bayesian Information Criterion (BIC) show that third-order polynomial fitting is optimal for the majority of spatial pixel positions, though the third-order coefficients are of a small magnitude at $\leq 10^{-10}$ nm pixel^{-3} (Fig. 10). Spectral distortion of the illuminated slit is $< \pm 0.75$ spectral pixel (CH_4, CO_2) and $< \pm 0.25$ spectral pixel (O_2), with expected largest distortion near the spatial pixel edges and the shortest wavelengths in the CO_2 band, albeit within acceptable limits (Fig. 10). Keystone is at a sub-pixel scale and negligible. Dispersion decreases with increasing wavelength, with the largest magnitude difference in the CO_2 band (Fig. 10). The CO_2 band exhibits a lower dispersion at spatial pixel edges. These disparate behaviors in the CO_2 band relative to the other spectral bands are expected due to the spectral design.

https://doi.org/10.5194/egusphere-2026-2675
Preprint. Discussion started: 21 May 2026

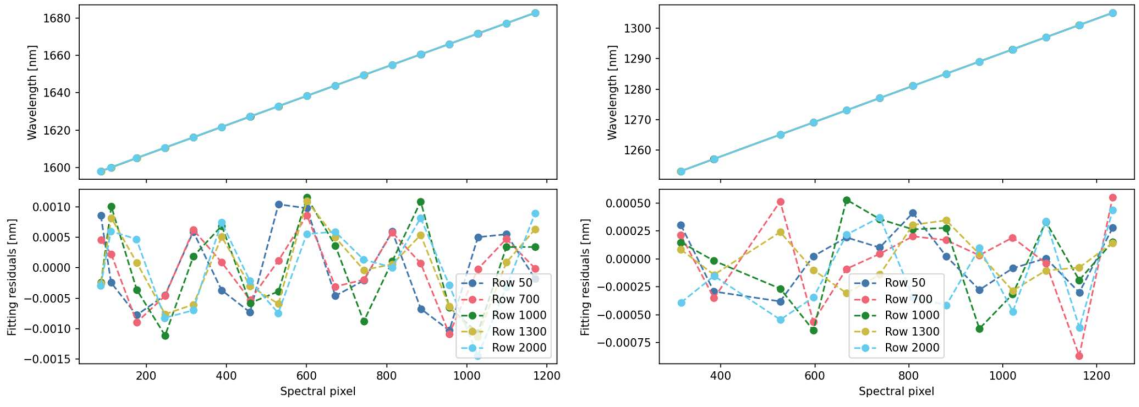

Figure 9: Wavelength calibration curves and fitting residuals for select spatial pixels that cover the usable illuminated spatial pixel extent for the CH_4 sensor (a) and O_2 sensor (b).

https://doi.org/10.5194/egusphere-2026-2675
Preprint. Discussion started: 21 May 2026

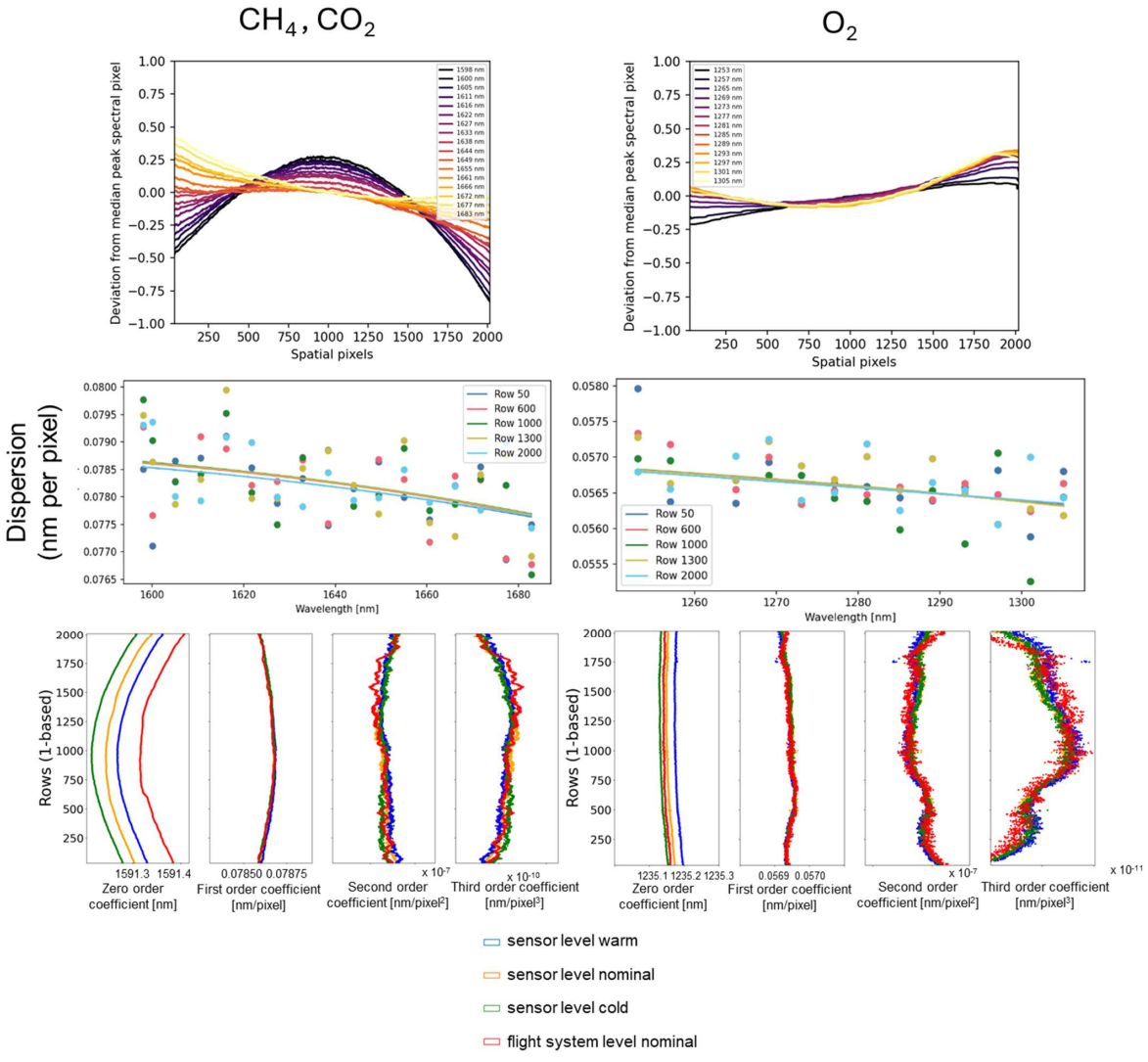

Figure 10: (Top) Spatial pixel pattern in deviation from median spectral pixel illustrates spectral distortion effects. (Middle) Global dispersion (lines) as a function of wavelength at CH_4 and CO_2 band cold sensor level (left) and O_2 band flight system level (right). Local dispersion as a function of wavelength is denoted by points. (Bottom) Wavelength calibration coefficients as a function of spatial pixel position for third-order polynomial fitting.

https://doi.org/10.5194/egusphere-2026-2675
Preprint. Discussion started: 21 May 2026

Sensor	Experiment	Prism temperature (°C)	Spectrometer temperature (°C)	Sensor objective element 1 temperature (°C)
CH_4	Sensor level goBack Warm	19.8	19.8	21.6
CH_4	Flight system level Nominal	19.6	19.6	NA
CH_4	Sensor level goBack Nominal	19.5	19.5	21.3
CH_4	Sensor level goBack Cold	19.3	19.3	21.0

Table 3. MethaneSAT CH_4 sensor pre-launch sensor level goBack and flight system level median component temperatures across all spatial ILS collects.

Sensor	Experiment	Prism temperature (°C)	Spectrometer temperature (°C)	Sensor objective element 1 temperature (°C)
O_2	Sensor level goBack Warm	19.8	19.8	21.6
O_2	Flight system level Nominal	19.5	19.5	NA
O_2	Sensor level goBack Nominal	19.6	19.5	21.3
O_2	Sensor level goBack Cold	19.3	19.3	21.0

Table 4. MethaneSAT O_2 sensor pre-launch sensor level goBack and flight system level median component temperatures across all spatial ILS collects.

First-order through third-order wavelength calibration coefficients are consistent across temperatures and calibration experiments, whereas the zero-order coefficient representing the wavelength shift varies with thermal conditions by ≤ 0.5 spectral pixels (Fig. 10). Prism temperatures are expected to correlate with wavelength grid shifts on the detector. Sensor level goBack prism temperatures are offset by close to the target ± 0.25 °C from nominal temperature (Tables 3 and 4). Flight system level prism temperatures are between warm and nominal sensor level goBack temperatures in the CH_4 sensor, whereas they are between nominal and cold sensor level goBack temperatures in the O_2 sensor. This suggests a slightly different thermal environment between experiments. We find that the order of the zero order wavelength coefficients is consistent with the order of O_2 sensor prism temperatures, but inconsistent for the CH_4 sensor (Table 3), suggesting that additional thermal environment factors contribute to the observed spectral shifts. We discuss this further with L2 fitted wavelength shifts in section 3.3.

https://doi.org/10.5194/egusphere-2026-2675
Preprint. Discussion started: 21 May 2026

3.3 On-orbit spectral calibration stability

Although the MethaneSAT design precluded direct on-orbit ISRF measurements, we assessed the on-orbit performance of the spectral calibration via other approaches. First, we conducted analyses to monitor the L2 retrieval impacts from potential changes in ISRFs between ground-based calibration and on-orbit conditions. We evaluated the impacts of different ISRF lookup tables representing three thermal conditions on the tabulated squeeze factor and wavelength shift fits at L2 (Chan Miller et al., 2024). The squeeze factor represents a stretching of the ISRF, corresponding to a uniform change in ISRF width. Chan Miller et al. (2024) and Staebell et al. (2021) demonstrated that including the squeeze factor parameter minimizes fitting residuals and retrieval cross-track biases for MethaneAIR. A squeeze factor of unity indicates that the on-orbit ISRF width matches the ground-based calibration derived ISRFs, and deviations from unity represent differences in ISRF widths between ground-based and on-orbit calibration. Squeeze factors greater than unity represent a narrower feature than prescribed by the ISRF table. Second-order ISRF shape changes due to thermal defocusing that potentially occurred on-orbit are not captured by this approach.

We focused on two MethaneSAT scenes collected over the Libya4 pseudo invariant calibration site (PICS) (Bacour et al., 2019) (~0.7 surface albedo) and the Condamine oil and gas production region in Australia (~0.3 surface albedo) (Table 5). These scenes were selected to sample a factor of 2.2 difference in surface albedo, minimal topographic features, and clear sky (cloud fraction <2%). Furthermore, most desert scenes are impacted by dust aerosols in the column, resulting in a high bias in fitted O_2 sensor-derived surface pressure relative to the prior (dp) in non-scattering retrievals (Chan Miller et al., 2024). We select scenes with dp < 15 hPa to minimize the impact of aerosol levels on L2 fitting metrics because this level of scattering is typically correctable by the proxy ratio (Chan Miller et al., 2024).

We observed positive deviations in squeeze factors when using sensor level goBack ISRFs, indicating on-orbit ISRFs were narrower than ISRFs derived from sensor-level goBack calibrations (Fig. 11). Fitted CO_2 and CH_4 vertical column densities and dry-air column-averaged CH_4 mole fractions (XCH_4) exhibited relatively small variations of ≤ 0.2% between retrievals using the four different ISRF lookup tables. L2 fitting residual RMS was consistent when using different temperature experiment ISRFs, except for 2% higher fitting residual RMS when using the sensor level warm ISRFs compared with the other ISRF look up tables. This indicates that the squeeze factor parameter accounts for most of the temperature difference impacts on retrievals. The CO_2 band squeeze factors exhibit relatively higher temperature sensitivity due to the instrument design not being optimized in the CO_2 band. Thermal defocusing effects that impact on-orbit ISRF widths relative to those during ground-based calibrations may be associated with spectrometer and objective temperatures (Tables 3 and 4). Across-track median CH_4 and CO_2 band squeeze factors using sensor level goBack ISRFs are in the same order as spectrometer and objective temperatures (Fig. 11). We observed small negative deviations in CH_4 sensor squeeze factors using the flight system level goBack ISRFs (Fig. 11). This is consistent with the 0.5 °C colder on-orbit sensor objective temperature (20.8 °C)

https://doi.org/10.5194/egusphere-2026-2675
Preprint. Discussion started: 21 May 2026

compared with the nominal flight system level goBack objective temperature (21.3 °C) (Table 3). Furthermore, on-orbit CH_4 sensor thermal defocusing was closest to that during cold sensor level goBack testing at 21.0°C (Tables 3 and 4; Fig. 11). Across-track median O_2 band squeeze factors are indistinguishable when using ISRFs from each of the four experiments, with variations dominated by residual ISRF FOV overlap artifacts.

We observe 2 to 3% higher positive deviation in squeeze factors at ~100 spatial pixels from each spatial pixel edge for a subset of ISRF temperature cases. This illumination edge artifact aligns with the PSF bezel edge scatter tail as well as the balancing of optical aberration (mainly focus) that varies between the spatial pixel center and edges. Spatial pixel variations in fitted XCH_4, vertical column densities, and fit residuals are not correlated with the narrower on-orbit spatial pixel edge ISRFs compared with those during ground-based calibrations. Finally, the corresponding wavelength shifts within L2 fits are 0.03 to 0.13 nm in the CH_4/CO_2 sensor and 0 to 0.045 nm in the O_2 sensor (Fig. 12). These shifts are consistent between the two scenes examined (only Libya 4 is depicted in Fig. 12 for brevity). The range and order of fitted wavelength shifts (Fig. 12) are also consistent with those for the zero-order wavelength calibration coefficients (Fig. 10).

For MethaneSAT spectral calibration, we chose to use the ISRF lookup tables corresponding to the minimum deviation in squeeze factors from unity, minimum spatial pixel edge artifacts, and with minimum fitting residuals. We use the cold sensor-level goBack ISRFs for CH_4 and CO_2 spectral fitting and the flight system level nominal temperature for O_2 band spectral fitting.

Target ID	Target Name	Number of scenes used in this study	Latitude center	Longitude center	Region description
24	Libya1	1	24.432396° N	13.349892° E	Saharan PICS
25	Libya4	9	28.563849° N	23.389872° E	Saharan PICS
42	Bowen Surat 1	2	27.336837° S	150.978265° E	Australia (oil and gas basin)
192	OC-0 Condamine	2	27.095863° S	150.020524° E	Australia (oil and gas basin)

Table 5. Target scene geographies used for L2 ISRF squeeze factor and wavelength shift analyses. Targets 42 and 192 represent nearly overlapping geographic areas that were shifted during the on-orbit mission.

https://doi.org/10.5194/egusphere-2026-2675
Preprint. Discussion started: 21 May 2026

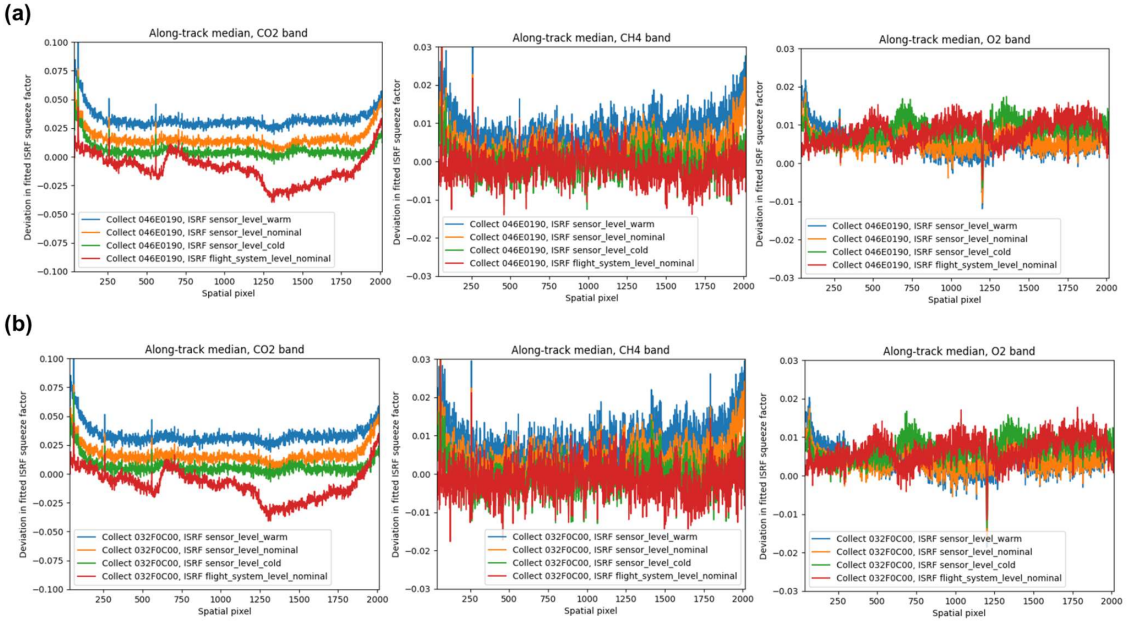

Figure 11: Spatial pixel pattern in on-orbit ISRF squeeze factors deviations from the reference of unity using four ISRF temperature and experimental iterations for (a) Libya4 scene collection on 22 November 2024 and (b) Condamine scene collection on 25 October 2024. Squeeze factors are fit separately for CH_4, CO_2 and O_2 spectral bands.

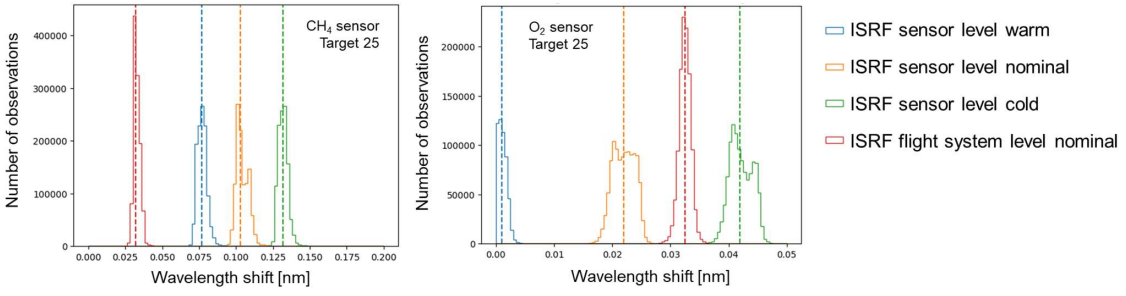

Figure 12: Fitted L2 wavelength shift spatial distributions for on-orbit Libya4 target 25 scene collected on 22 November 2024 using four ISRF temperature and experimental iterations. Dashed vertical lines represent the mean value of each distribution.

https://doi.org/10.5194/egusphere-2026-2675
Preprint. Discussion started: 21 May 2026

Second, we characterized the on-orbit temporal stability of L2 ISRF squeeze factors and fitted wavelength shifts in representative on-orbit scenes over time. We used 14 on-orbit MethaneSAT scenes from four target regions (Table 5), covering four seasons from September 2024 through June 2025. The temporal coverage gap between January to May 2025 was due to a combination of orbit raising, system resets, target selection changes, and clouds. Across the time series of the MethaneSAT data collection, the temporal variations in spatial pixel median ISRF squeeze factor deviations and wavelength shifts are smaller than their distributions across spatial pixels (Figs 13 and 14). Spatial pixel median squeeze factor deviations varied by 0.1% (CH_4 band) and <0.4% (CO_2 and O_2 bands) (Figs. 13 and 14). Spatial pixel distributions of squeeze factor deviations and wavelength shifts demonstrate relatively stable spectral calibration compared with ground-based calibration across expected on-orbit thermal conditions (Figs 13 and 14). Spatial pixel median wavelength shifts varied by 6.5 pm (5%) in the CH_4 sensor (Fig. 13) and 14.5 pm (48%) in the O_2 sensor (Fig. 14). These on-orbit wavelength shift drifts are below those observed during sensor level goBack calibration, within the one spectral pixel requirement over a 90-day period, and did not correlate with cloud or shadow fractions.

To further assess the small observed L2 metric temporal drifts, we also examine the on-orbit sensor objective temperatures that were measured separately for each sensor. Sensor objective temperatures should correlate with focus at the slit. We intentionally slightly reduced focus at the slit to partially mitigate instantaneous ISRF narrowing when observing significant albedo gradients in the along-track direction that result in a partially illuminated slit (Hummel et al., 2021). There is a small (0.001) seasonal drift in median CH_4 band squeeze factor deviation, though this is not observed in the CO_2 band. Monthly median variations in on-orbit objective temperatures were 0.08°C in both sensors (Figs. 13 and 14), within the thermistor heater control cycle of $< \pm 0.05$°C. CH_4 sensor objective temperatures exhibited maximum temperatures during northern hemisphere summer, though the variations are within that of the heater control cycle. These temperature variations are much smaller in magnitude than pre-launch thermal modeling that suggested a much larger 0.5 °C seasonal cycle with maximum temperatures during the Northern Hemisphere winter due to sun-angle variations. This is consistent with the intention for a conservative pre-launch thermal model. Therefore, the ISRF temperature sensitivity analyses in section 3.2 represent a wider range of thermal conditions than that observed on-orbit. Overall, our observations demonstrate small on-orbit thermal changes were associated with small drifts in on-orbit ISRF shapes and spectral shifts in the on-orbit wavelength grid.

https://doi.org/10.5194/egusphere-2026-2675
Preprint. Discussion started: 21 May 2026

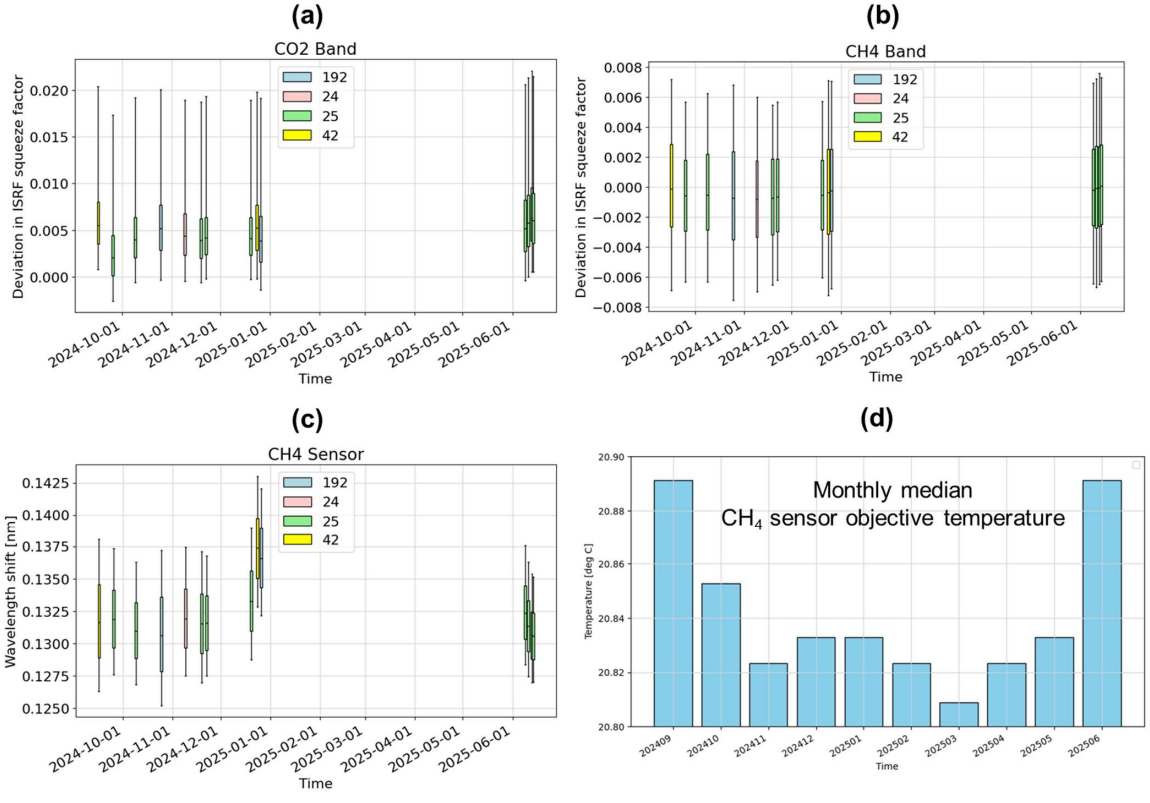

Figure 13: Time series of (a) CO_2 and (b) CH_4 band along-track median on-orbit spatial pixel distributions of ISRF squeeze factor deviation in select clear sky, bright scenes. (c) Time series of CH_4 sensor (inclusive of both CO_2 and CH_4 bands) wavelength shifts in select clear sky, bright scenes. (a-c) Boxes represent interquartile ranges and whiskers represent 5 and 95 percentiles of the spatial pixel distributions. 95% confidence intervals for these distributions are small and within the thickness of the median lines. (d) Monthly median CH_4 on-orbit objective temperatures based on all on-orbit scene data collection periods.

https://doi.org/10.5194/egusphere-2026-2675
Preprint. Discussion started: 21 May 2026

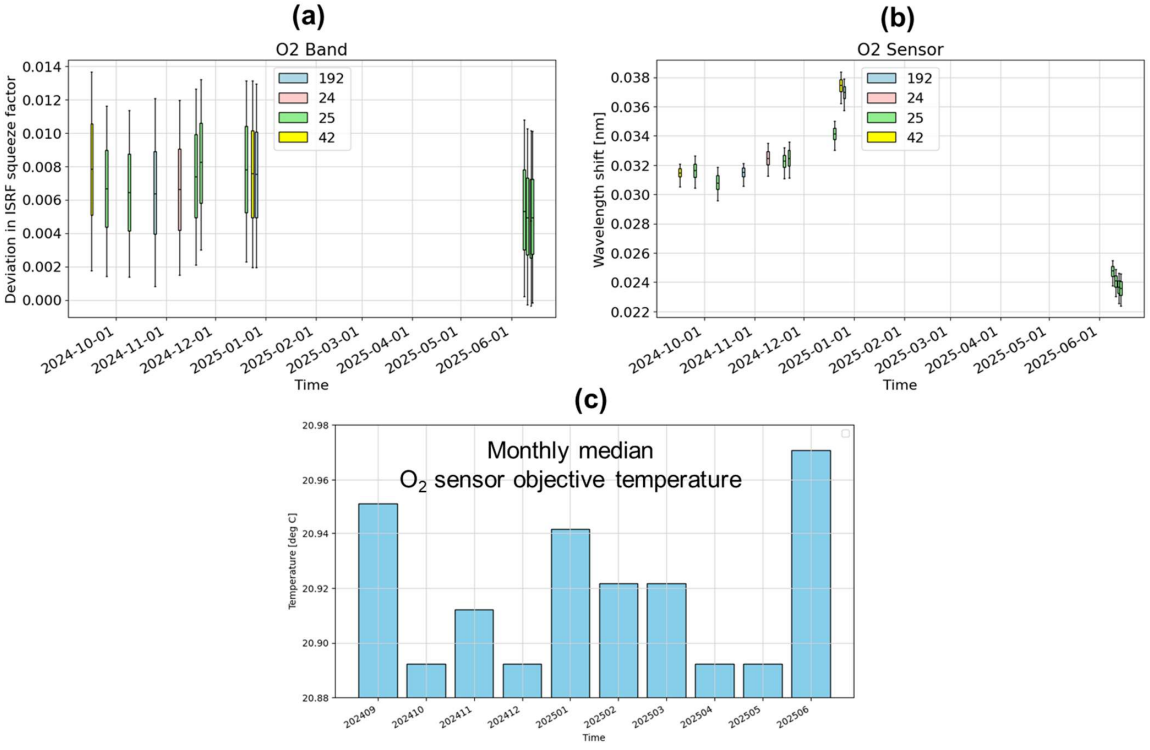

Figure 14. Time series of O_2 sensor along-track median on-orbit spatial pixel distributions of (a) ISRF squeeze factor deviations and (b) wavelength shifts in select clear sky, bright scenes. (a-b) Boxes represent interquartile ranges and whiskers represent 5 and 95 percentiles of the spatial pixel distributions of each parameter. 95% confidence intervals for these distributions are small and within the thickness of the median lines. (c) Monthly median O_2 on-orbit objective temperatures are based on all on-orbit scene data collection periods.

4 Conclusions & Implications

We report novel spectral calibration methods to characterize the MethaneSAT ISRFs and wavelength calibration. We conclude that these methods account for MethaneSAT's larger field of view and accurately characterize ISRF patterns in the spatial pixel and spectral directions during ground-based calibrations. The ISRF estimation methods presented in this study were robust in capturing small differences across multiple pre-launch calibration efforts. We found relatively small temperature sensitivities (<5%) for ISRF shapes, with the largest relative differences in the CO_2 band. Finally, on-orbit time series of L2

https://doi.org/10.5194/egusphere-2026-2675
Preprint. Discussion started: 21 May 2026

retrieval metrics across multiple seasons suggest that ISRFs were relatively stable compared with ground-based calibration across expected on-orbit thermal conditions during the 14-month on-orbit MethaneSAT mission.

Several improvements in future satellite imaging spectrometer missions could facilitate refined spectral calibration methods. For instance, improvements in the spatial pixel overlap between spatial fields of view and characterizing slit illumination edge artifacts (e.g. stray-light features that impact measured line shapes) could provide smoother ISRF estimates across the field of view. Micro-wavelength step and range specification requirements could be revisited to balance oversampling needs with experimental time constraints. Solar absorption spectra measurements during ground-based and/or on-orbit operation, as well as on-orbit limb measurement of airglow could be further explored for directly characterizing ISRF drifts over time and differences between ground-based and on-orbit defocusing effects. Collecting point spread functions at different thermal conditions could provide opportunities to characterize thermal impacts on stray-light effects. Improvements could also target a more consistent thermal environment between sensor and flight system level ground-based calibrations. Finally, improving characterization of bezel scatter effects at spatial edges at multiple wavelengths and spectral pixels could facilitate quantitative analysis for correction of this effect to maximize the usable spatial field of view. Our results have important implications for the on-orbit performance and calibration of MethaneSAT L2 retrievals, and could inform other, similar satellite imaging spectrometer greenhouse gas monitoring missions.

Code availability

The underlying algorithms for this study can be accessed at https://github.com/Kang-Sun-CfA/Methane/blob/master/l1/MethaneSAT_ISRF.py.

Data availability

The ISRF lookup tables, stray-light kernels, and MethaneSAT on-orbit L1 and L2 data used in this study can be accessed at https://dataverse.harvard.edu/previewurl.xhtml?token=f50af482-e6eb-4781-9746-fbfccee75b80 (Franklin, 2026).

Author contributions

DJM, NL, KS, CCM, SC, EW, and JEF developed the methodology; DJM, BL, SR, CCM, NL, SA, SC, TK, PS, BF, TM, NL produced input data; DJM, KS, JEF, BL, SR, CCM, SC analyzed the data; DJM, KS, BL, XL, NL, SR wrote and edited the manuscript; all co-authors reviewed the manuscript.

https://doi.org/10.5194/egusphere-2026-2675
Preprint. Discussion started: 21 May 2026

Competing interests

The authors declare that they have no conflicts of interest.

Acknowledgements

We are grateful for the support of and valuable discussions with Chris O'Dell. We are especially grateful to the BAE Systems, Inc. teams who conducted the calibration measurements used in this study. We thank Steven P. Hamburg, Millie Chu Baird, and Peter Vedder for their leadership of the MethaneSAT mission. We are grateful to Norton Allen, Joshua S. Benmergui, Apisada Chulakadabba, Lisa Fullerton, Shauda Islam, Maya Nasr, Jasna Pittman, Maryann Sargent, and the entire MethaneSAT science and data processing platform teams for their contributions. We acknowledge the Center for Computational Research at the University at Buffalo, the Information Technology Services at Center for Astrophysics | Harvard & Smithsonian, and the FASRC Cannon cluster supported by the FAS Division of Science Research Computing Group at Harvard University for providing scientific computing services. We are also grateful to Google, Inc. for cloud computing resources.

Financial support

This work was funded by MethaneSAT LLC grants awarded to the Research Foundation of State University of New York at Buffalo and Harvard University. Funding for MethaneSAT and MethaneAIR activities was provided in part by Anonymous, Arnold Ventures, The Audacious Project, Ballmer Group, Bezos Earth Fund, The Children's Investment Fund Foundation, Heising-Simons Family Fund, King Philanthropies, Robertson Foundation, Skyline Foundation and Valhalla Foundation. For a more complete list of funders, please visit www.methanesat.org.

References

Bacour, C.; Briottet, X.; Bréon, F.-M.; Viallefont-Robinet, F.; Bouvet, M. Revisiting Pseudo Invariant Calibration Sites (PICS) Over Sand Deserts for Vicarious Calibration of Optical Imagers at 20 km and 100 km Scales. Remote Sens. 2019, 11, 1166. https://doi.org/10.3390/rs11101166.

Chan Miller, C., Roche, S., Wilzewski, J. S., Liu, X., Chance, K., Souri, A. H., Conway, E., Luo, B., Samra, J., Hawthorne, J., Sun, K., Staebell, C., Chulakadabba, A., Sargent, M., Benmergui, J. S., Franklin, J. E., Daube, B. C., Li, Y., Laughner, J. L., Baier, B. C., Gautam, R., Omara, M., and Wofsy, S. C.: Methane retrieval from MethaneAIR using the CO_2 proxy approach:

https://doi.org/10.5194/egusphere-2026-2675
Preprint. Discussion started: 21 May 2026

a demonstration for the upcoming MethaneSAT mission, Atmos. Meas. Tech., 17, 5429–5454, https://doi.org/10.5194/amt-17-5429-2024, 2024.

Chulakadabba, A., Sargent, M., Lauvaux, T., Benmergui, J. S., Franklin, J. E., Chan Miller, C., Wilzewski, J. S., Roche, S., Conway, E., Souri, A. H., Sun, K., Luo, B., Hawthrone, J., Samra, J., Daube, B. C., Liu, X., Chance, K., Li, Y., Gautam, R., Omara, M., Rutherford, J. S., Sherwin, E. D., Brandt, A., and Wofsy, S. C.: Methane point source quantification using MethaneAIR: a new airborne imaging spectrometer, Atmos. Meas. Tech., 16, 5771–5785, https://doi.org/10.5194/amt-16-5771-2023, 2023.

Conway, E. K., A. H. Souri, J. Benmergui, K. Sun, X. Liu, C. Staebell, C. Chan Miller, J. E. Franklin, J. Samra, J. S. Wilzewski, S. Roche, B. Luo, A. Chulakadabba, M. Sargent, J. Hohl., B. Daube, I. Gordon, K. Chance, S. C. Wofsy, Level0-to-Level1B processor for MethaneAIR, Atmos. Meas. Tech., 17, 1347–1362, https://doi.org/10.5194/amt-17-1347-2024, 2024.

Crisp, D., Pollock, H. R., Rosenberg, R., Chapsky, L., Lee, R. A. M., Oyafuso, F. A., Frankenberg, C., O'Dell, C. W., Bruegge, C. J., Doran, G. B., Eldering, A., Fisher, B. M., Fu, D., Gunson, M. R., Mandrake, L., Osterman, G. B., Schwandner, F. M., Sun, K., Taylor, T. E., Wennberg, P. O., and Wunch, D.: The on-orbit performance of the Orbiting Carbon Observatory-2 (OCO-2) instrument and its radiometrically calibrated products, Atmos. Meas. Tech., 10, 59–81, https://doi.org/10.5194/amt-10-59-2017, 2017.

El Haouari, J., Gaucel, J.-M., Pittet, C., Tourneret, J.-Y., and Wendt, H.: In-flight estimation of instrument spectral response functions using sparse representations, Atmos. Meas. Tech., 18, 2573–2590, https://doi.org/10.5194/amt-18-2573-2025, 2025.

Franklin, Jonathan, 2026, "MethaneSAT instrument spectral response functions during pre-launch calibration and on-orbit performance", https://doi.org/10.7910/DVN/60HCFC, Harvard Dataverse, DRAFT VERSION.

Hummel, T., Meister, C., Keim, C., Krauser, J., and Wenig, M.: Slit homogenizer introduced performance gain analysis based on the Sentinel-5/UVNS spectrometer, Atmos. Meas. Tech., 14, 5459–5472, https://doi.org/10.5194/amt-14-5459-2021, 2021.

Lee, R.A.M. et al., "Preflight Spectral Calibration of the Orbiting Carbon Observatory 2," in IEEE Transactions on Geoscience and Remote Sensing, vol. 55, no. 5, pp. 2499-2508, May 2017, doi: 10.1109/TGRS.2016.2645614.

Luo, B., et al., MethaneSAT L0 to L1B processor and in-Flight Calibration and Performance, 4.12, presented at *21st International Workshop on Greenhouse Gas Measurements from Space (IWGGMS-21),* Takamatsu, Japan, 9-12 June, 2025 (Oral), https://www.nies.go.jp/soc/doc/IWGGMS-21/oral/4.12_Luo_public.pdf.

https://doi.org/10.5194/egusphere-2026-2675
Preprint. Discussion started: 21 May 2026

MacKay, K., Benmergui, J., Williams, J. P., Omara, M., Himmelberger, A., Sargent, M., Warren, J. D., Miller, C. C., Roche, S., Zhang, Z., Franklin, J., Guanter, L., Wofsy, S., and Gautam, R.: Assessment of methane emissions from US onshore oil and gas production using MethaneAIR measurements, Atmos. Chem. Phys., 26, 1179–1192, https://doi.org/10.5194/acp-26-1179-2026, 2026.

Nasr, M., J. E. Franklin, J. Benmergui and S. C. Wofsy, "MethaneSAT On-Orbit Lunar Calibrations Planning," *2025 IEEE Aerospace Conference*, Big Sky, MT, USA, 2025, pp. 1-9, doi: 10.1109/AERO63441.2025.11068427.

Rohrschneider, R.R., Wofsy, S., Franklin, J.E., Benmergui, J., Soto, J., & Davis, S.B. (2021). The MethaneSAT Mission, 35th Annual Small Satellite Conference, 2021.

Staebell, C., Sun, K., Samra, J., Franklin, J., Chan Miller, C., Liu, X., Conway, E., Chance, K., Milligan, S., and Wofsy, S.: Spectral calibration of the MethaneAIR instrument, Atmos. Meas. Tech., 14, 3737–3753, https://doi.org/10.5194/amt-14-3737-2021, 2021.

Sun, K., Liu, X., Nowlan, C. R., Cai, Z., Chance, K., Frankenberg, C., Lee, R. A. M., Pollock, R., Rosenberg, R., and Crisp, D.: Characterization of the OCO-2 instrument line shape functions using on-orbit solar measurements, Atmos. Meas. Tech., 10, 939–953, https://doi.org/10.5194/amt-10-939-2017, 2017.

Tanimoto, H., Matsunaga, T., Someya, Y. et al. The greenhouse gas observation mission with Global Observing SATellite for Greenhouse gases and Water cycle (GOSAT-GW): objectives, conceptual framework and scientific contributions. Prog Earth Planet Sci 12, 8 (2025). https://doi.org/10.1186/s40645-025-00684-9.

Taylor, T.E., et al., OCO-3 early mission operations and initial (vEarly) XCO_2 and SIF retrievals, Remote Sensing of Environment, Volume 251, 2020, 112032, ISSN 0034-4257, https://doi.org/10.1016/j.rse.2020.112032.

Tol, P. J. J., van Kempen, T. A., van Hees, R. M., Krijger, M., Cadot, S., Snel, R., Persijn, S. T., Aben, I., and Hoogeveen, R. W. M.: Characterization and correction of stray light in TROPOMI-SWIR, Atmos. Meas. Tech., 11, 4493–4507, https://doi.org/10.5194/amt-11-4493-2018, 2018.

van Hees, R. M., Tol, P. J. J., Cadot, S., Krijger, M., Persijn, S. T., van Kempen, T. A., Snel, R., Aben, I., and Hoogeveen, Ruud W. M.: Determination of the TROPOMI-SWIR instrument spectral response function, Atmos. Meas. Tech., 11, 3917–3933, https://doi.org/10.5194/amt-11-3917-2018, 2018.

https://doi.org/10.5194/egusphere-2026-2675
Preprint. Discussion started: 21 May 2026

van Kempen, T. A., van Hees, R. M., Tol, P. J. J., Aben, I., and Hoogeveen, R. W. M.: In-flight calibration and monitoring of the Tropospheric Monitoring Instrument (TROPOMI) short-wave infrared (SWIR) module, Atmos. Meas. Tech., 12, 6827–6844, https://doi.org/10.5194/amt-12-6827-2019, 2019.

Warren, J. D., Sargent, M., Williams, J. P., Omara, M., Miller, C. C., Roche, S., MacKay, K., Manninen, E., Chulakadabba, A., Himmelberger, A., Benmergui, J., Zhang, Z., Guanter, L., Wofsy, S., and Gautam, R.: Sectoral contributions of high-emitting methane point sources from major US onshore oil and gas producing basins using airborne measurements from MethaneAIR, Atmos. Chem. Phys., 25, 10661–10675, https://doi.org/10.5194/acp-25-10661-2025, 2025.

Williams, J. P., Benmergui, J., Knapp, M., Omara, M., Himmelberger, A., Kyzivat, E., Weatherby, K., Lyke, B., Warren, J., MacKay, K., Ayvazov, S., Russi, M., LoFaso, N., Melendez, T., Miller, C. C., Roche, S., Sargent, M., Franklin, J., Nasr, M., Zhang, Z., Miller, D. J., Luo, B., Guanter, L., Hamburg, S. P., Wofsy, S. C., and Gautam, R.: Methane intensity and emissions across major oil and gas basins and individual jurisdictions using MethaneSAT observations, Atmos. Chem. Phys., 26, 5961–5981, https://doi.org/10.5194/acp-26-5961-2026, 2026.